

# Contrastive Counterfactual Visual Explanations With Overdetermination

Adam White\*, Kwun Ho Ngan\*

James Phelan, Saman Sadeghi Afgeh, Kevin Ryan

Constantino Carlos Reyes-Aldasoro, Artur d'Avila Garcez

City Data Science Institute

City, University of London, London, EC1V 0HB, UK

## Abstract

A novel explainable AI method called *CLEAR Image* is introduced in this paper. *CLEAR Image* is based on the view that a satisfactory explanation should be contrastive, counterfactual and measurable. *CLEAR Image* explains an image's classification probability by contrasting the image with a corresponding image generated automatically via adversarial learning. This enables both salient segmentation and perturbations that faithfully determine each segment's importance. *CLEAR Image* was successfully applied to a medical imaging case study where it outperformed methods such as Grad-CAM and LIME by an average of 27% using a novel pointing game metric. *CLEAR Image* excels in identifying cases of 'causal overdetermination' where there are multiple patches in an image, any one of which is sufficient by itself to cause the classification probability to be close to one.

## 1 Introduction

Data-driven AI for Computer Vision can achieve high levels of predictive accuracy, yet the rationale behind these predictions is often opaque. This paper proposes a novel explainable AI (XAI) method called *CLEAR Image* that seeks to reveal the causal structure implicitly modelled by an AI system, where the causes are an image's segments and the effect is the AI system's classification probability. *CLEAR Image* is based on the philosopher James Woodward's seminal analysis of causal explanation (Woodward 2003), which develops Judea Pearl's manipulationist account of causation (Pearl 2009). Together they constitute the dominant account of explanation in the philosophy of science. We argue that a successful explanation for an AI system should be contrastive, counterfactual and measurable.

According to Woodward, to explain an event  $E$  is "to provide information about the factors on which it depends and exhibit how it depends on those factors". This requires a *causal equation* to describe the causal structure responsible for generating the event. The causal equation must support a set of counterfactual instances that serve to illustrate this structure, and to answer a set of 'what-if-things-had-been-different' questions. It follows that, contrary to current XAI counterfactual methods (Verma, Dickerson, and Hines

2020), stating only a set of counterfactual instances without their supporting equation(s) does not constitute a satisfactory explanation.

A contrastive explanation seeks to answer the question 'Why  $E$  rather than  $F$ ?'  $F$  is referred to as  $E$ 's foil and it comes from a contrast class of events that were alternatives to  $E$ , but which did not happen (Van Fraassen et al. 1980). An explanation can thereby identify the causes that led to  $E$  occurring rather than  $F$ , even though the relevant contrast class to which  $F$  belongs is often not explicitly conveyed.

For Woodward, all causal claims are counterfactual and contrastive: 'to causally explain an outcome  $E$  is always to explain why it, rather than some alternative, occurred'. In XAI research, counterfactuals usually state instead minimal changes needed to achieve the desired foil  $F$ .

The 'causal overdetermination' of an event occurs when two or more sufficient causes of this event happen. A standard example from the philosophy literature is about the soldiers in a firing squad simultaneously shooting a prisoner, with each shot being sufficient to kill the prisoner. The death of the prisoner is causally overdetermined. This causal structure may well be ubiquitous in learning systems. For example, there may be multiple patches in a medical image, any of which being sufficient in itself to cause a classification probability close to one. To the best of our knowledge, *CLEAR Image* is the first XAI method capable of identifying causal overdetermination.

*CLEAR Image* explains an image's classification probability by contrasting the image with a corresponding GAN generated image. However, a GAN's difference mask should only be a starting point for segmentation and explanation. As we will illustrate, the segments identified from a difference mask can vary greatly in their relevance to a classification; furthermore other segments critical to the classification can often be absent from the mask. *CLEAR Image* therefore uses a novel segmentation method that combines information from the difference mask, the original image and from the classifier's behavior. *CLEAR Image* then follows a process of perturbation, whereby the input values are changed, and the change in outcome is observed to produce a regression equation. The regression equation is used to determine the contribution each segment makes to the classification probability. *CLEAR Image* identifies counterfactuals and measures the fidelity of its explanation against the clas-

\*lead authors

Corresponding author: Adam.White@city.ac.uk  
Under Review. All rights reserved.

sifier.

The contribution of this paper is three-fold. We introduce an XAI method that:

- generates contrastive, counterfactual and measurable explanations outperforming established XAI methods in challenging image domains;
- uses a GAN to generate a foil and explicitly explains an image’s classification relative to that foil.
- is capable of identifying causal overdetermination.

CLEAR *Image* was evaluated in two case studies, both involving overdetermination. The first using a multifaceted synthetic dataset, the second using chest X-rays. CLEAR *Image* outperformed XAI methods such as LIME and Grad-CAM by an average of 31% on the synthetic dataset and 27% on the X-ray dataset based on a pointing game metric defined in this paper for the case of multiple targets. CLEAR *Image* is based on an earlier XAI method, (Counterfactual Local Explanations via Regression), which was designed for tabular data (White and d’Avila Garcez 2020). Our code will be made available on GitHub.

The remainder of the paper is organised as follows: Section 2 defines the relevant notation and background. Section 3 discusses the immediate related work. Section 4 introduces the CLEAR *Image* method and algorithms. Section 5 details the experimental setup and discusses results. Section 6 concludes the paper and indicates directions for future work.

## 2 Background

### 2.1 Key Notation

This paper adopts the following notation: let the instance  $x$  be an image, and  $m$  be a machine learning system that maps  $x$  to class label  $l$  with probability  $y$ . Let  $x$  be partitioned into  $S$  segments (regions)  $\{s_1, \dots, s_n\}$ . Let any variable with a prime subscript  $'$  be the variable from the GAN-generated image e.g.  $x'$  is the GAN generated image derived from  $x$ , and maps to class  $l$  with probability  $y'$ .

### 2.2 Explanation by Perturbation

Methods such as Occlusion (Zhou et al. 2016), Extremal Perturbation (Fong, Patrick, and Vedaldi 2019), FIDO (Chang et al. 2018), LIME (Ribeiro, Singh, and Guestrin 2016) and Kernel SHAP (Lundberg and Lee 2017) use perturbation to evaluate which segments of an image  $x$  are most responsible for  $x$ ’s classification probability  $y$ . The underlying idea is that the contribution that a segment  $s_i$  makes to  $y$  can be determined by substituting it with an uninformative segment  $s'_i$ , where  $s'_i$  may be either grey, black or blurred (Zhou et al. 2016; Fong, Patrick, and Vedaldi 2019; Ribeiro, Singh, and Guestrin 2016) or in-painted without regard to any contrast class (Chang et al. 2018). There are three key problems with using perturbed images to explain a classification:

1. A satisfactory explanation must have a relevant foil  $F$ ; it must answer ‘Why  $E$  rather than  $F$ ?’ None of the above methods does this. Their foils are instead images of uninformative segments.

2. The substitution may fail to identify the contribution that  $s_i$  makes to  $y$ . For example, replacing  $s_i$  with black pixels can take the entire image outside of the classifier’s training distribution. By contrast, blurring or uninformative in-painting might result in  $s'_i$  being too similar to  $s_i$  resulting in the contribution of  $s_i$  being underestimated.
3. A segmentation needs to be relevant to its explanatory question. Current XAI perturbation approaches produce radically different segmentations. FIDO and Extremal Perturbation identify ‘optimal’ segments that, when substituted by an uninformative segment, maximally affect the classification probability; by contrast, LIME uses a texture/intensity/colour algorithm (e.g. Quickshift).

CLEAR *Image* uses GAN generated images to address each of these problems: (i) its foil is a GAN generated image  $x'$  belonging to a contrast class selected by the user. (ii) inpainting with segments derived from  $x'$  enables better estimation of each segment’s contribution to the difference between probabilities  $y$  and  $y'$ . (iii) the differences between  $x$  and  $x'$  are used to guide the segmentation.

## 3 Related Work

The XAI methods most relevant to this paper can be broadly grouped into three types:

**(i) Gradient-based methods:** These provide saliency maps by backpropagating an error signal from a neural network’s output to either the input image or an intermediate layer. Simonyan, Vedaldi, and Zisserman (2014) use the derivative of a class score for the image to assign an importance score to each pixel. Kumar, Wong, and Taylor’s **C**lass-**E**nhanced **A**ttention **R**esponse (2017) uses backpropagation to visualise the most dominant classes; this should not be confused with our method. A second approach modifies the backpropagation algorithm to produce sharper saliency maps, e.g. by suppressing the negative flow of gradients. Prominent examples of this approach (Springenberg et al. 2014; Zeiler and Fergus 2014) have been found to be invariant to network re-parameterization or the class predicted (Adebayo et al. 2018; Nie, Zhang, and Patel 2018). A third approach (Selvaraju et al. 2017; Chattopadhyay et al. 2018) uses the product of gradients and activations starting from a late layer. In Grad-CAM (Selvaraju et al. 2017), the product is clamped to only highlight positive influences on class scores.

**(ii) Perturbation based methods:** LIME and Kernel SHAP generate a dataset of perturbed images, which feeds into a regression model, which then calculates segment importance scores (LIME) or Shapley Values (Kernel SHAP). These bear some similarity to CLEAR *Image* but key differences include: they do not use a GAN generated image, do not identify counterfactuals and do not report fidelity. Extremal Perturbation uses gradient descent to determine an optimal perturbed version of an image that, for a fixed area, has the maximal effect on a network’s output whilst guaranteeing that the selected segments are smooth. FIDO use variational Bernoulli drop to find a minimal set of segments that would change an image’s class. In contrast

to LIME, Kernel SHAP and Extremal Perturbation, FIDO uses a GAN to in-paint segments with 'plausible alternative values', however, these values are not generated so as to belong to a chosen contrast class. Furthermore, segment importance scores are not produced.

(iii) **GAN difference methods:** Generative adversarial network (GAN) (Goodfellow et al. 2014) has been widely applied for synthetic image generation. Difference masks are created by subtracting a GAN generated image  $x'$  from its original image  $x$ . Image translation through direct mapping of the original image to its target class has gained popularity, such as CycleGAN (Zhu et al. 2017) and StarGAN (Choi et al. 2018). StarGAN V2 (Choi et al. 2020) introduced a style vector for conditional image translation and produced high quality images over a diverse set of target conditions. These models, however, do not keep the translation minimal and make modification even for intra-domain translation. Fixed-point GAN (Siddiquee et al. 2019) introduced an identity loss penalizing any deviation of the image during intra-domain translation. This aims to enhance visual similarity with the original image. DeScarGAN (Wolleb, Sandkühler, and Cattin 2020) adopts this loss function in its own GAN architecture and has outperformed Fixed-point GAN in their case study for Chest X-Ray pathology identification and localisation.

CLEAR *Image* builds on the strengths of these XAI methods but also addresses key shortcomings. As already outlined, it uses a 'GAN-augmented' segmentation algorithm rather than just a difference mask. Next, methods such as LIME assume that a classification probability is a simple linear addition of its causes. This is incorrect for cases of causal overdetermination, and CLEAR *Image* therefore uses a sigmoid function (see section 4). Finally, our experiments confirm that prominent XAI methods often fail to identify the most relevant regions of an image, CLEAR *Image* therefore measures the fidelity of its explanations.

## 4 The CLEAR *Image* Method

CLEAR *Image* is a model-agnostic XAI method that explains the classification of an image made by any classifier. It requires both image  $x$  and a contrast image  $x'$  generated by a GAN. CLEAR *Image* segments  $x$  into  $\{s_1, \dots, s_n\} \in S$  and then applies the same segmentation to  $x'$  creating  $\{s'_1, \dots, s'_n\} \in S'$ . CLEAR *Image* determines the contributions that different subsets of  $S$  make to  $y$  by substituting with the corresponding segments of  $S'$ . CLEAR *Image* is GAN agnostic, allowing the user to choose the GAN architecture most suitable to their project. A set of 'image-counterfactuals'  $\{c_1 \dots c_k\}$  is also identified.

**Definition 1** An *image-counterfactual*  $c_j$  from  $l$  to  $l'$  is an image resulting from a change in the values of one or more segments of  $x$  to their corresponding values in  $S'$  such that  $\text{class}(m(x)) = l$ ,  $\text{class}(m(c_j)) = l'$  and  $l \neq l'$ . The change is minimal in that if any of the changed segments had remained at its original value, then  $\text{class}(m(x)) = \text{class}(m(c_j))$ .

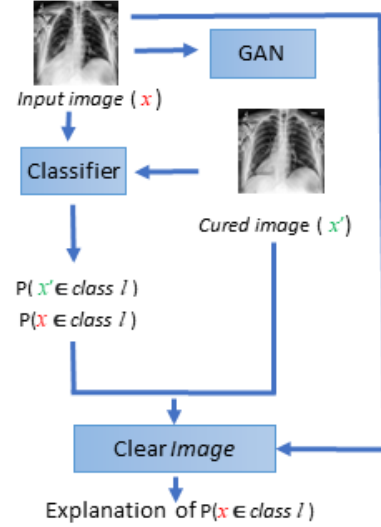


Figure 1: The CLEAR *Image* pipeline

CLEAR *Image* uses a regression equation to quantify the contribution that individual segments make to  $y$ . It then measures the fidelity of its regression by comparing the classification probability resulting from each  $c_j$  with an estimate obtained from the regression equation.

**Definition 2** *Counterfactual-regression fidelity error*  
 $= | \text{regression equation}(c_j) - y_{c_j} |$ .

The following steps generate an explanation of prediction  $y$  for image  $x$ :

1. **GAN-Augmented segmentation algorithm.** First, an initial set of segments  $S_h$  is identified by applying a high threshold to the intensities in the difference mask between  $x$  and  $x'$ . The high threshold is determined using multi-Otsu or can be user-specified; if necessary, CLEAR *Image* will progressively lower this threshold until at least two segments are created. Second, an additional set of segments  $S_l$  is determined by applying a low threshold to the remaining unsegmented regions of the difference mask and applying a combination of connected component labelling, erosion and the 'over-segmenting' Felzenszwalb algorithm (which includes a 'minimum segment size' parameter). The combined set of segments  $\{S_h, S_l\}$  is checked to see if any individual segment is an image-counterfactual. If not,  $S_l$  is recreated, but with the 'minimum segment size' being increased. This continues until either an image-counterfactual is identified, or a user defined minimum number of segments is reached (See Algorithm 2). In some cases, a successful segmentation can be achieved by only applying a high threshold. Our synthetic case study is an example of this, as the images do not have fine-grained details. In such cases, the user can specify that the second part of the GAN-Augmented algorithm is not used. Additionally, CLEAR *Image*'s modular structure enables the user to adjust the segmentation algorithm if, for example, a different thresholding

- or over-segmentation algorithm suits their domain better.
- Determine  $x$ 's image-counterfactuals. A dataset of perturbed images is created by selectively replacing segments of  $x$  with the corresponding segments of  $x'$ . A separate image is created for every combination in which either 1, 2, 3, or 4 segments are replaced. Each perturbed image is then passed through  $m$  to determine its classification probability. All image-counterfactuals involving changes in up to 4 segments are then identified.
  - Generate a regression dataset of perturbed images. Perturbed images are created by randomly replacing segments of  $x$  with the corresponding segments of  $x'$ , with their classification probabilities determined by  $m$ . These are added to the dataset created in step 2. If necessary, a simple genetic algorithm is then used to generate additional images around the decision boundary.
  - Perform a stepwise logistics regression. This is carried out using a  $\{0,1\}$  representation of each segment of each image in the regression dataset. Each segment  $s$  in  $x$  is represented by 1, and each segment  $s'$  in  $x'$  by 0. The observations corresponding to image-counterfactuals (from step 2) are given a high weighting and act as soft constraints on the subsequent regression.
  - Calculate segment importance scores. These are the regression coefficients for each segment from step 4.
  - Identify cases of causal overdetermination.
  - Measure the fidelity of the regression by calculating fidelity errors (see Figure 2) and goodness of fit statistics.
  - Iterate to best explanation. Because CLEAR *Image* produces fidelity statistics, its parameters can be changed to achieve a better trade-off between interpretability and fidelity. Key parameters include the number of segments to include in the regression equation.

---

**Algorithm 1: CLEAR *Image***


---

**input** :  $x$  - input image,  
 $x'$  - contrast image,  
 $m$  - AI classifier.  
 $S, S' \leftarrow \text{GAN\_Augmented\_Segmentation}(x, x', m)$   
 $D \leftarrow \text{Create\_Synthetic\_Data}(S, S', m)$   
 $C \leftarrow \text{Find\_Counterfactuals}(S, S', m)$   
 $r \leftarrow \text{Find\_Regression\_Equation}(D, C)$   
 $G \leftarrow \text{Extract\_Segment\_Scores}(r)$   
 $O \leftarrow \text{Find\_Overdetermination}(r)$   
 $e \leftarrow \text{Calculate\_Fidelity}(C, r)$   
**return**  $\text{expl} = \langle G, C, r, O, e \rangle$

---

For CLEAR *Image* an explanation (expl) is a tuple  $\langle G; C; r; O, e \rangle$ , where  $G$  are segment importance scores,  $C$  are image-counterfactuals,  $r$  is a regression equation,  $O$  are the causes resulting in overdetermination, and  $e$  are fidelity errors. Figure 2 shows an extract from a CLEAR report.

The causal overdetermination of an effect occurs when multiple sufficient causes of that effect occur. By default, CLEAR *Image* only reports sufficient causes which each consist of a single segment belonging to  $S$ . Substituting a sufficient cause with its corresponding member in  $S'$  guar-

---

**Algorithm 2: GAN\_Augmented\_Segmentation**


---

**input** :  $x$  - diseased image,  $x'$  - contrast image,  
 $m$  - AI classifier  
 $highT, lowT \leftarrow \text{Get\_Thresholds}(x, x')$   
 $S_h, S_l \leftarrow \text{Diff\_masks}(x, x', highT, lowT)$   
 $S_l \leftarrow \text{Largest\_Conn\_Comps\_Erosion}(S_l, x)$   
 $N_s \leftarrow \text{Num\_Seg}(S_h, S_l)$   
 //  $maxSeg, minSeg$  are user inputs  
**if**  $N_s < maxSeg$  **then**  
    $minSize = 250$  pixels  
    $N_c \leftarrow \text{Num\_Seg\_Counterfact}(m, S_h, S_l)$   
   **while**  $N_c = 0$  and  $minSeg \leq N_s \leq maxSeg$  **do**  
      $S_l \leftarrow \text{Apply\_Felz}(S_l)$   
      $N_s \leftarrow \text{Num\_Seg}(S_h, S_l)$   
      $N_c \leftarrow \text{Num\_Seg\_Counterfact}(m, S_h, S_l)$   
      $minSize += 25$  pixels  
 $S, S' \leftarrow \text{Combine\_segments}(S_h, S_l, x')$   
**return**  $S, S'$

---

antees the effect. In philosophy of science, it is generally taken that for an effect to be classified as overdetermined, it should be narrowly defined, such that all the sufficient causes have the same, or very nearly the same impact (Paul 2009). For the case studies, the effect is defined as  $p(x \in \text{diseased}) > 0.99$ , though the user may choose a different probability threshold. A sufficient cause changes a GAN generated healthy image to a diseased image. This is in the opposite direction to CLEAR *Image*'s counterfactuals which 'cure' a diseased image. Sufficient causes can be read off from CLEAR *Image*'s regression equation. Using the example in Figure 2 with the logistic formula, a classification probability of  $> 0.99$  requires  $w^T x > 4.6$ . The GAN healthy image corresponds to all the binary segment variables being equal to zero. Hence,  $w^T x$  is equal to the intercept value of -4.9, giving a probability of  $(1 + \exp^{4.9})^{-1} \approx 0.01$ . If a segment  $s'_i$  is now replaced by  $s_i$ , the corresponding binary variable changes to 1. Hence if segment 9 is infilled, then  $Seg09 = 1$  and  $w^T x = 6.8$  (i.e.  $11.7 - 4.9$ ). Similarly, infilling just segment 11 will make  $w^T x > 4.6$ . Either substitution is sufficient to guarantee  $w^T x > 4.6$ , irrespective of any other changes that could be made to the values of the other segment variables. Hence segments 9 & 11 are each a sufficient cause and there is overdetermination.

## 5 Experimental Investigation

There are two case studies, the first using a synthetic dataset, the second analyzing pleural effusion X-rays taken from the CheXpert dataset (Irvin et al. 2019). Transfer learning was used to train both a VGG-16 with batch normalization and a DenseNet-121 classifier for each dataset. CLEAR *Image* was evaluated against Grad-CAM, Extremal Perturbations and LIME. The evaluation consisted of both a qualitative comparison of saliency maps and a comparison of pointing game and intersection over union (IoU) scores. CLEAR *Image*'s fidelity errors were also analysed (none of the other XAI methods measures fidelity).

Prediction to be explained: Xray: 18470 has probability 1.0 of effusion

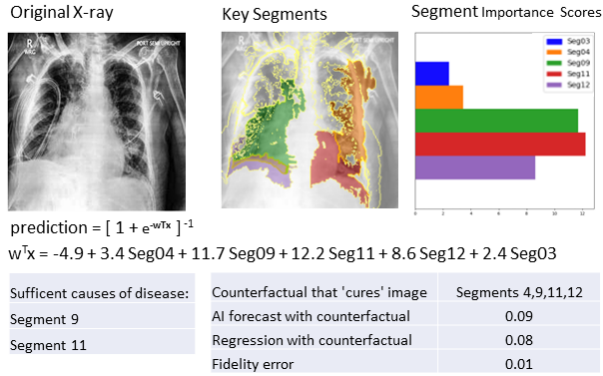


Figure 2: Extracts from a CLEAR *Image* report. The report states that the segments 4,9,11 & 12 all need to be infilled to flip the classification of the X-ray to ‘healthy’. According to CLEAR’s logistic regression equation infilling these segments changes the probability of the X-ray being classified as ‘effusion’ to 0.08. However when these segments were actually infilled and passed through the classifier, the probability changed to 0.09, hence the fidelity error is 0.01.

## 5.1 Datasets

The synthetic dataset’s images share some key characteristics found in medical imaging including: (i) different combinations of features leading to the same classification (ii) irrelevant features. All images (healthy and diseased) contain: a set of concentric circles, a large and a small ellipse. An image is ‘diseased’ if either: (1) the small ellipse is thin-lined, and the large ellipse contains a square or (2) there is a triangle, and the large ellipse contains a square. The dataset is adapted from (Wolleb, Sandkühler, and Cattin 2020).

CheXpert is a dataset of Lung X-Ray with automated pathological label extraction through radiology reports, consisting of 224,316 radiographs of 65,240 patients in total. Images were extracted just for the classes ‘pleural effusion’ and ‘no finding’. Mis-classified images and images significantly obstructed by supporting devices were manually filtered. A random frontal X-ray image per patient was collected. In total, a dataset of 2,440 images was used in this work for model training, validation and testing. Appendix A details of the data preparation process. A hospital doctor provided the ground truth annotation to the X-ray images with pleural effusion for our case study.

## 5.2 GAN-Based Image Generation

To generate contrastive images, DeScarGAN and StarGAN-V2 have been deployed as the network architectures for the synthetic dataset and the CheXpert dataset respectively. The use of these established GAN networks demonstrates how the generated contrastive images can aid in the overall CLEAR *Image* pipeline. Default training hyperparameters were applied unless otherwise stated. Details of model training and hyperparameters can be found in Appendix B. The source image was applied as input for the Style Encoder instead of a specific reference image for StarGAN-V2. This

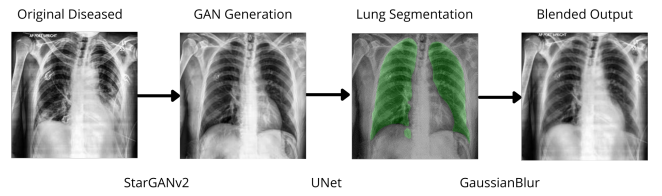


Figure 3: The post-processing of GAN generated image.

ensures the generated style mimics that of the input source images. StarGAN-V2 is also not locally constrained (i.e. the network will modify all pixels in an image related to the targeted class which will include irrelevant spurious regions of the image). A post generation lung space segmentation step using a pre-trained U-Net model was implemented and the original diseased lung space is replaced with the generated image with a Gaussian Blur process to fuse the edge effect as shown in Figure 3. This reduces the feature identification space within the lung space. It is an advantage of the CLEAR *Image* pipeline that it is possible to use pre-processing to focus the explanation on the relevant parts of  $x$ . As we will show, XAI methods that do not take a contrast image as part of their input can sometimes identify parts of  $x$  which are known to be irrelevant as being responsible for a classification.

## 5.3 Evaluation Metrics

This paper uses two complementary metrics to evaluate XAI methods. Both require annotated images identifying ‘target’ regions that should be critical to their classification. A pointing game produces the first metric, which measures how successfully a saliency map ‘hits’ an image’s targets. Previously pointing games have been designed for cases where (i) images have single targets (ii) the saliency maps have a maximum intensity point (Fong, Patrick, and Vedaldi 2019; Zhang et al. 2018). By contrast, this paper’s case studies have multiple targets, and the pixels within each CLEAR *Image* segment have the same value. We, therefore, formulated a novel pointing game. The pointing game partitions a ‘diseased’ image into 49 square segments,  $P = \{p_1 \dots p_{49}\}$  and identifies which squares contain each of the targets. The corresponding saliency map is also partitioned, and each square is allocated a score equal to the average intensity of that square’s pixels  $Q = \{q_1 \dots q_{49}\}$ . The pointing game then starts with the  $q_i$  of highest intensity and determines if the corresponding  $p_i$  contains a relevant feature. A successful match is a ‘hit’ and an unsuccessful match is a ‘miss’. This process continues until every target has at least one hit. The score for an image is the number of hits over the number of hits plus misses. Pseudocode is provided in Algorithm 3.

The second metric is IoU. In order to apply IoU each pixel in a saliency map is classified as being ‘salient’ if it is above the 70<sup>th</sup> percentile of intensities in that map. IoU then measures the overlap between the ‘salient’ pixels  $pix^{salient}$  and the pixels belonging to the image’s targets  $pix^{target}$ :  $IOU = (pix^{salient} \cap pix^{target}) / (pix^{salient} \cup pix^{target})$ .



Both metrics are useful but have counterexamples. For example, IoU would give too high a score to a saliency map that strongly overlapped with a large image target but completely missed several smaller targets that were also important to a classification. However, applied together, the two metrics provide a good indication of an XAI's performance.

### Algorithm 3: Pointing Game

---

```

input :  $x$  - input image,  $A$  - annotated features
         $w$  - XAI saliency map
 $P_A \leftarrow \text{Square\_Idx\_of\_Each\_Feature}(A, x)$ 
 $Q \leftarrow \text{Average\_Intensity\_Each\_Square}(w)$ 
 $Q' \leftarrow \text{Square\_Idx\_Sort\_Highest\_Intensity}(Q)$ 
 $hits \leftarrow 0$ ;  $misses \leftarrow 0$ ;  $h_A \leftarrow \text{False}$ 
foreach  $q'_i \in Q'$  do
    // starting with highest
    foreach  $a_j \in A$  do
        if  $q'_i \in P_{a_j}$  then // square idx match
             $hits \leftarrow hits + 1$ ;  $h_{a_j} \leftarrow \text{True}$ 
        else
             $misses \leftarrow misses + 1$ 
        if  $\forall a_j (h_{a_j} = \text{True})$  then
            // exit once all features hit
            break
return  $\langle hits, misses \rangle$ 

```

---

## 5.4 Experimental Runs

CLEAR *Image* was run using logistic regression with the Akaike information criterion; full testing and parameter values can be found in Appendix B. The test datasets consisted of 95 annotated X-rays and 100 synthetic images. The average running time for CLEAR *Image* was 20 seconds per image for the synthetic dataset and 38 seconds per image for the CheXpert dataset, running on a Windows i7-8700 RTX 2070 PC. Default parameter values were used for the other XAI methods, except for the following beneficial changes: Extremal Perturbations was run with 'fade to black' perturbation type, and using areas  $\{0.025, 0.05, 0.1, 0.2\}$  with the masks summed and a Gaussian filter applied. LIME was run using Quickshift segmentation with kernel sizes 4 and 20 for CheXpert and synthetic dataset respectively.

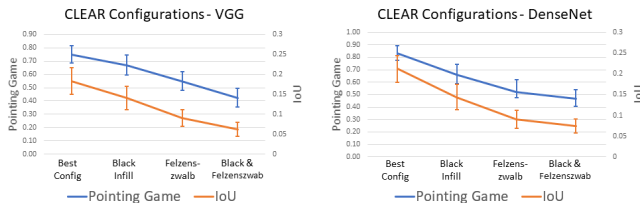


Figure 4: Evaluation metrics (with 95% confidence intervals) for different configurations of CLEAR with CheXpert.

## 5.5 Experimental Results

Figure 4 illustrates some of the benefits of using the 'Best Configuration': GAN-augmented segmentation and infilling

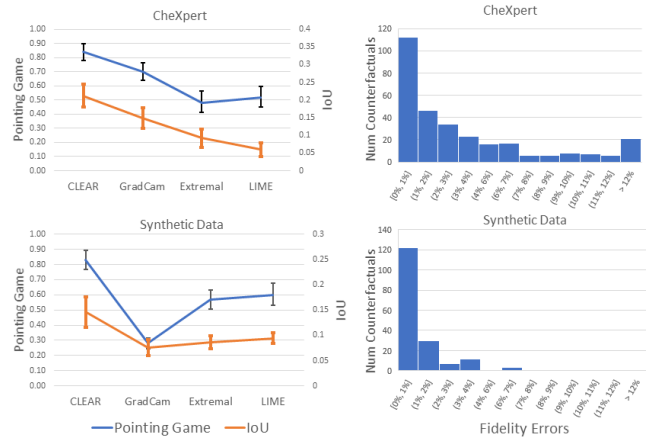


Figure 5: Evaluation metrics (with 95% confidence intervals) and fidelity errors for DenseNet models

using  $x'$ . This is compared with (i) segmenting with Felzenszwalb and infilling with  $x'$  (ii) segmenting with GAN-augmented but infilling with black patches (iii) segmenting Felzenszwalb, infilling black patches. CLEAR *Image* outperforms the other XAI methods on both datasets (Figure 5). Furthermore, its fidelity errors are low, indicating that the regression coefficients are accurate for the counterfactually important segments. Figure 6 illustrates how CLEAR *Image*'s use of GAN-augmented leads to a better explanations than just using a difference mask. CLEAR *Image*'s performance was similar for VGG-16 and DenseNet; therefore only the DenseNet results will be presented unless otherwise stated.

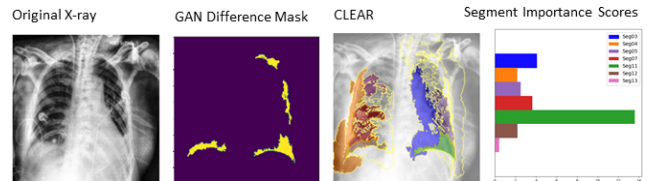


Figure 6: GAN-Augmented Segmentation versus GAN difference mask. The difference mask identifies 4 segments but when CLEAR *Image* perturbs these, the 2 nearest to the top were found to be irrelevant. Of the other 2 segments, CLEAR *Image* identifies the segment it colors green to be far more important to the classification probability.

CLEAR *Image*'s regression equation was able to capture the relatively complex causal structure that generated the synthetic dataset. A square (SQ) is a *necessary but insufficient* cause for being diseased. An image is labelled as diseased if there is also either a triangle (TR) or the small ellipse is thin-lined (TE). When SQ, TR and TE are all present in a single image, there is a type of overdetermination in which TR and TE are each a sufficient cause *relative* to the 'image with SQ already present'. Figure 7 shows an example. As before, a healthy image corresponds to the binary segment variables equalling one and a classification prob-

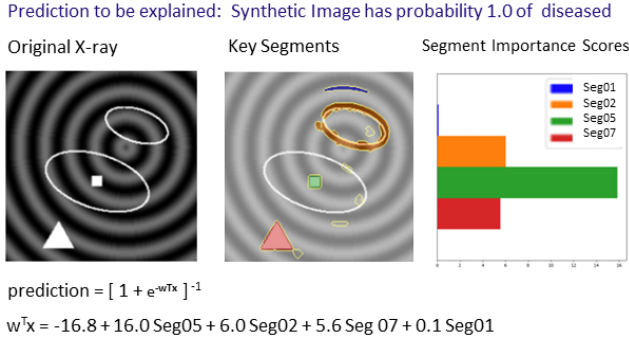


Figure 7: Extracts from a CLEAR *Image* report for a synthetic image. The regression equation shows that Seg05 is a necessary but insufficient cause of the X-ray being diseased.

ability of  $> 0.99$  requires  $w^T x > 4.6$ . This can only be achieved by Seg 5 (corresponding to SQ) plus at least one of Seg 2 or Seg 7 (TE, TR) being set to 1 (i.e. being present). Figure 8 compares the saliency maps for synthetic data.

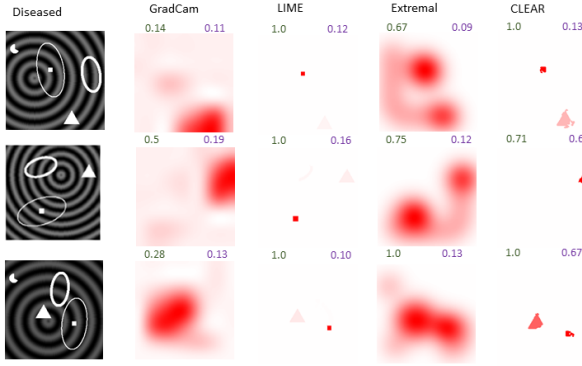


Figure 8: Comparison of XAI methods on synthetic data. The pointing game scores are shown in green and the IoU scores are in purple. The significance of a patch is indicated by its red intensity.

For the CheXpert dataset, Figure 9 illustrates how CLEAR *Image* allows for a greater appreciation of the pathology compared to ‘broad-brush’ methods such as GradCAM (please see Appendix A1 for further saliency maps). Nevertheless, the IoU scores highlight that the segmentation can be further improved. For CheXpert’s counterfactuals, only 5% of images did not have a counterfactual with four or fewer  $s'$  segments. Most images required several  $s'$  segments to be infilled before its classification flipped to ‘cured’, 17% required one segment, 30% with two segments, 24% with three segments and 24% with four segments. 17% of the X-rays were found to be causally overdetermined.

## 6 Conclusion and Future Work

A key reason for CLEAR *Image*’s outperformance of other XAI methods is its novel use of GANs. It recognises that a difference mask is only the starting point for an explanation,

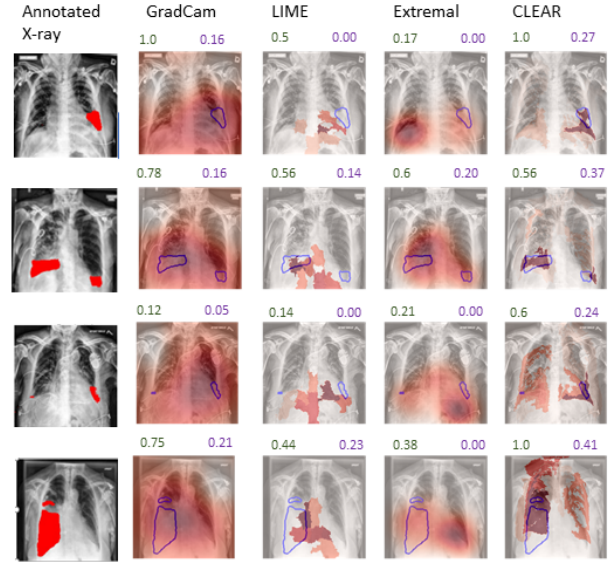


Figure 9: Comparison of XAI methods on X-ray. The pointing game scores are shown in green and the IoU scores are in purple. The significance of a patch is indicated by the intensity of red against the blue outlined annotated ground truth.

and instead uses a GAN image both for infilling and as an input into its own segmentation algorithm.

As AI systems for image data are increasingly adopted in society, understanding their implicit causal structures has become paramount. Yet the explanations provided by XAI methods cannot always be trusted, as the differences in Figure 9’s saliency maps show. It is therefore critical that an XAI method measures its own fidelity. By ‘knowing when it does not know’, it can alert the user when its explanations are unfaithful.

A limitation of CLEAR *Image* is that it first requires training a GAN, which can be a challenging process. Another possible limitation could be the understandability of CLEAR *Image* to non-technical users. However, its reports can be suitably tailored, e.g. only showing saliency maps, lists of counterfactuals and cases of overdetermination.

We have shown that CLEAR *Image* can illuminate cases of causal overdetermination. Many other types of causal structure may also be ubiquitous in AI. For example, causal pre-emption and causal clustering are well documented within the philosophy of science (Baumgartner 2009; Schaffer 2004). The relevance of these to XAI will be a future area of work. A user study should also be carried out. However these are time/resource consuming and need to be devised carefully by experts within specific domains of application if they are to produce sound, reliable results. Instead, we focus on objective measures and evaluations of XAI research which in our view must precede any user study. Future work will also focus on improving segmentation, e.g. by introducing domain-specific constraint parameters for GANs, to minimise the modifications of specified attributes (e.g. changes in the heart for lung X-ray image generation).

## References

- Adebayo, J.; Gilmer, J.; Muelly, M.; Goodfellow, I.; Hardt, M.; and Kim, B. 2018. Sanity checks for saliency maps. *arXiv preprint arXiv:1810.03292*.
- Baumgartner, M. 2009. Inferring causal complexity. *Sociological methods & research*, 38(1): 71–101.
- Chang, C.-H.; Creager, E.; Goldenberg, A.; and Duvenaud, D. 2018. Explaining image classifiers by counterfactual generation. *arXiv preprint arXiv:1807.08024*.
- Chattopadhyay, A.; Sarkar, A.; Howlader, P.; and Balasubramanian, V. N. 2018. Grad-cam++: Generalized gradient-based visual explanations for deep convolutional networks. In *2018 IEEE Winter Conference on Applications of Computer Vision (WACV)*, 839–847. IEEE.
- Choi, Y.; Choi, M.; Kim, M.; Ha, J.-W.; Kim, S.; and Choo, J. 2018. Stargan: Unified generative adversarial networks for multi-domain image-to-image translation. In *Proceedings of the IEEE conference on computer vision and pattern recognition*, 8789–8797.
- Choi, Y.; Uh, Y.; Yoo, J.; and Ha, J.-W. 2020. StarGAN v2: Diverse Image Synthesis for Multiple Domains. In *2020 IEEE/CVF Conference on Computer Vision and Pattern Recognition (CVPR)*, 8185–8194.
- Fong, R.; Patrick, M.; and Vedaldi, A. 2019. Understanding deep networks via extremal perturbations and smooth masks. In *Proceedings of the IEEE/CVF International Conference on Computer Vision*, 2950–2958.
- Goodfellow, I.; Pouget-Abadie, J.; Mirza, M.; Xu, B.; Warde-Farley, D.; Ozair, S.; Courville, A.; and Bengio, Y. 2014. Generative adversarial nets. In *Advances in neural information processing systems*, 2672–2680.
- Irvin, J.; Rajpurkar, P.; Ko, M.; Yu, Y.; Ciurea-Ilcus, S.; Chute, C.; Marklund, H.; Haghighi, B.; Ball, R.; Shpanskaya, K.; Seekins, J.; Mong, D. A.; Halabi, S. S.; Sandberg, J. K.; Jones, R.; Larson, D. B.; Langlotz, C. P.; Patel, B. N.; Lungren, M. P.; and Ng, A. Y. 2019. CheXpert: A Large Chest Radiograph Dataset with Uncertainty Labels and Expert Comparison. *arXiv:1901.07031*.
- Kumar, D.; Wong, A.; and Taylor, G. W. 2017. Explaining the unexplained: A class-enhanced attentive response (clear) approach to understanding deep neural networks. In *Proceedings of the IEEE Conference on Computer Vision and Pattern Recognition Workshops*, 36–44.
- Lundberg, S. M.; and Lee, S.-I. 2017. A unified approach to interpreting model predictions. In *Advances in Neural Information Processing Systems*, 4765–4774.
- Nie, W.; Zhang, Y.; and Patel, A. 2018. A theoretical explanation for perplexing behaviors of backpropagation-based visualizations. In *International Conference on Machine Learning*, 3809–3818. PMLR.
- Paul, L. A. 2009. Counterfactual theories. *The Oxford handbook of causation*, 158–184.
- Pearl, J. 2009. *Causality: Models, Reasoning and Inference*. New York, NY, USA: Cambridge University Press, 2nd edition.
- Ribeiro, M. T.; Singh, S.; and Guestrin, C. 2016. Why Should I Trust You? Explaining the Predictions of Any Classifier. In *Proc. ACM SIGKDD 2016, KDD '16*, 1135–1144. New York, NY, USA: ACM. ISBN 978-1-4503-4232-2.
- Schaffer, J. 2004. Trumping preemption. *The Journal of Philosophy*, 97(4): 165–181.
- Selvaraju, R. R.; Cogswell, M.; Das, A.; Vedantam, R.; Parikh, D.; and Batra, D. 2017. Grad-cam: Visual explanations from deep networks via gradient-based localization. In *Proceedings of the IEEE international conference on computer vision*, 618–626.
- Siddiquee, M. M. R.; Zhou, Z.; Tajbakhsh, N.; Feng, R.; Gotway, M. B.; Bengio, Y.; and Liang, J. 2019. Learning fixed points in generative adversarial networks: From image-to-image translation to disease detection and localization. In *Proceedings of the IEEE International Conference on Computer Vision*, 191–200.
- Simonyan, K.; Vedaldi, A.; and Zisserman, A. 2014. Deep inside convolutional networks: Visualising image classification models and saliency maps. In *In Workshop at International Conference on Learning Representations*. Citeseer.
- Springenberg, J. T.; Dosovitskiy, A.; Brox, T.; and Riedmiller, M. 2014. Striving for simplicity: The all convolutional net. *arXiv preprint arXiv:1412.6806*.
- Van Fraassen, B. C.; et al. 1980. *The scientific image*. Oxford University Press.
- Verma, S.; Dickerson, J.; and Hines, K. 2020. Counterfactual explanations for machine learning: A review. *arXiv preprint arXiv:2010.10596*.
- White, A.; and d’Avila Garcez, A. 2020. Measurable Counterfactual Local Explanations for Any Classifier. In *ECAI 2020*, 2529–2535. IOS Press.
- Wolleb, J.; Sandkühler, R.; and Cattin, P. C. 2020. DeScarGAN: Disease-Specific Anomaly Detection with Weak Supervision. In *International Conference on Medical Image Computing and Computer-Assisted Intervention*, 14–24. Springer.
- Woodward, J. 2003. *Making things happen: a theory of causal explanation*. Oxford, England: Oxford University Press. ISBN 9780195189537.
- Zeiler, M. D.; and Fergus, R. 2014. Visualizing and understanding convolutional networks. In *European conference on computer vision*, 818–833. Springer.
- Zhang, J.; Bargal, S. A.; Lin, Z.; Brandt, J.; Shen, X.; and Sclaroff, S. 2018. Top-down neural attention by excitation backprop. *International Journal of Computer Vision*, 126(10): 1084–1102.
- Zhou, B.; Khosla, A.; Lapedriza, A.; Oliva, A.; and Torralba, A. 2016. Learning deep features for discriminative localization. In *Proceedings of the IEEE conference on computer vision and pattern recognition*, 2921–2929.
- Zhu, J.-Y.; Park, T.; Isola, P.; and Efros, A. A. 2017. Unpaired image-to-image translation using cycle-consistent adversarial networks. In *Proceedings of the IEEE international conference on computer vision*, 2223–2232.



## A Supplemental results for CheXpert dataset and associated data pre-processing

### A.1 Supplementary qualitative results

Additional qualitative results for the CheXpert dataset are presented in Figures 10 & 11 where the most important segments (regions) identified by each XAI method is matched against the annotated ground truth. These are the pixels of saliency maps that are above the 70th percentile in intensity (i.e. the segments used to calculate the IoU scores). Figure 10 shows the results for the DenseNet model while Figure 11 presents the results for the VGG model. These results have demonstrated higher precision using CLEAR Image in identifying significant segment matching against the annotated ground truth in comparison to other XAI methods. These two figures provide the qualitative comparison to supplement the results presented in Figure 5 where CLEAR Image outperforms other XAI methods.

### A.2 Data Pre-Processing

CheXpert has a total of 14 pathological observations, including ‘No Finding’ are labelled through an automated rule-based labeller from text radiology reports. For each observation, the Stanford team has classified each radiograph as either negative (0), uncertain (-1) or positive (1). Other metadata includes gender, age, X-ray image projection and presence of supporting devices.

In this study, this dataset (v1.0) was applied for the model development of a binary classification task to demonstrate the capability of CLEAR Image as an explainable AI framework. An initial filtering process of the metadata was applied for the two classes used in the study - (1) Diseased with Pleural Effusion and (2) Healthy (This is assumed to be X-ray images with no findings and no positive observations in any of the pathological conditions). To minimise potential complication with other pathological conditions, X-ray images with only positive in pleural effusion were used with other pathological categories either as negative/blank.

A review of the filtered images also identified that the dataset was curated with some images having significant artefacts that can hamper model training performance. Figure 12 presents some of these images in both diseased and healthy categories. Many of them consist of artefacts from image capturing and processing (e.g. image distortion, orientation, low resolutions or miscalibration). Some images were also significantly obstructed by limbs or support devices. Some healthy images were also wrongly labelled according to a hospital doctor. A secondary manual filtering was conducted to remove any identified images with artefacts.

The 2440 selected were split approximately 80/10/10 for the training/validation/testing. The images were also resized to 256 x 256 as the input into the classification model and generative adversarial network (GAN) as described in Section 5. Figure 13 presents some of the typical images in the final dataset for both diseased and healthy categories.

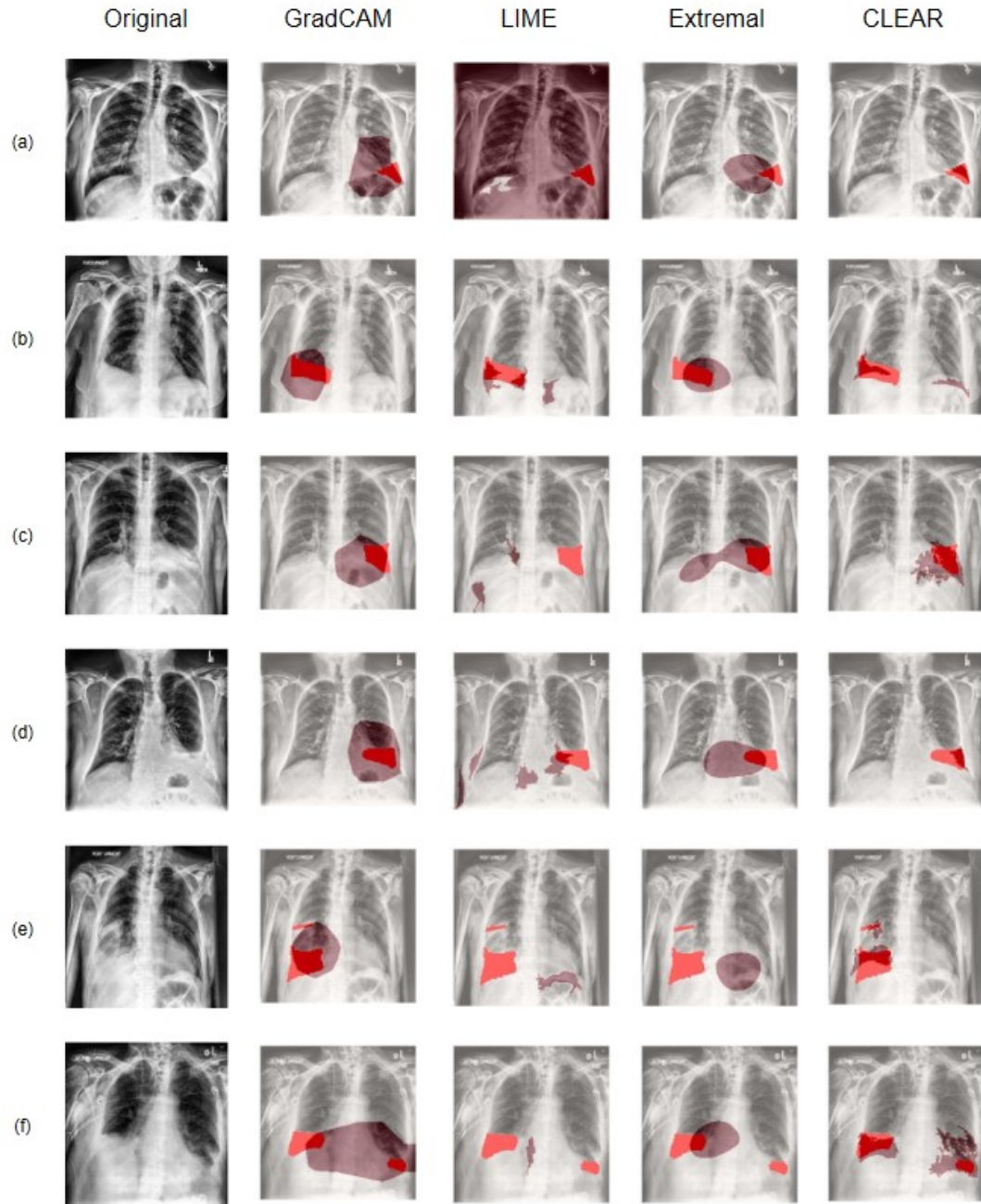


Figure 10: Representative comparative examples of the identified important segments of a DenseNet-based image classification model (Val Acc: 98.8%) for pleural effusion using (i) CLEAR *Image*, (ii) Grad-CAM, (iii) Extremal Perturbation and (iv) LIME.

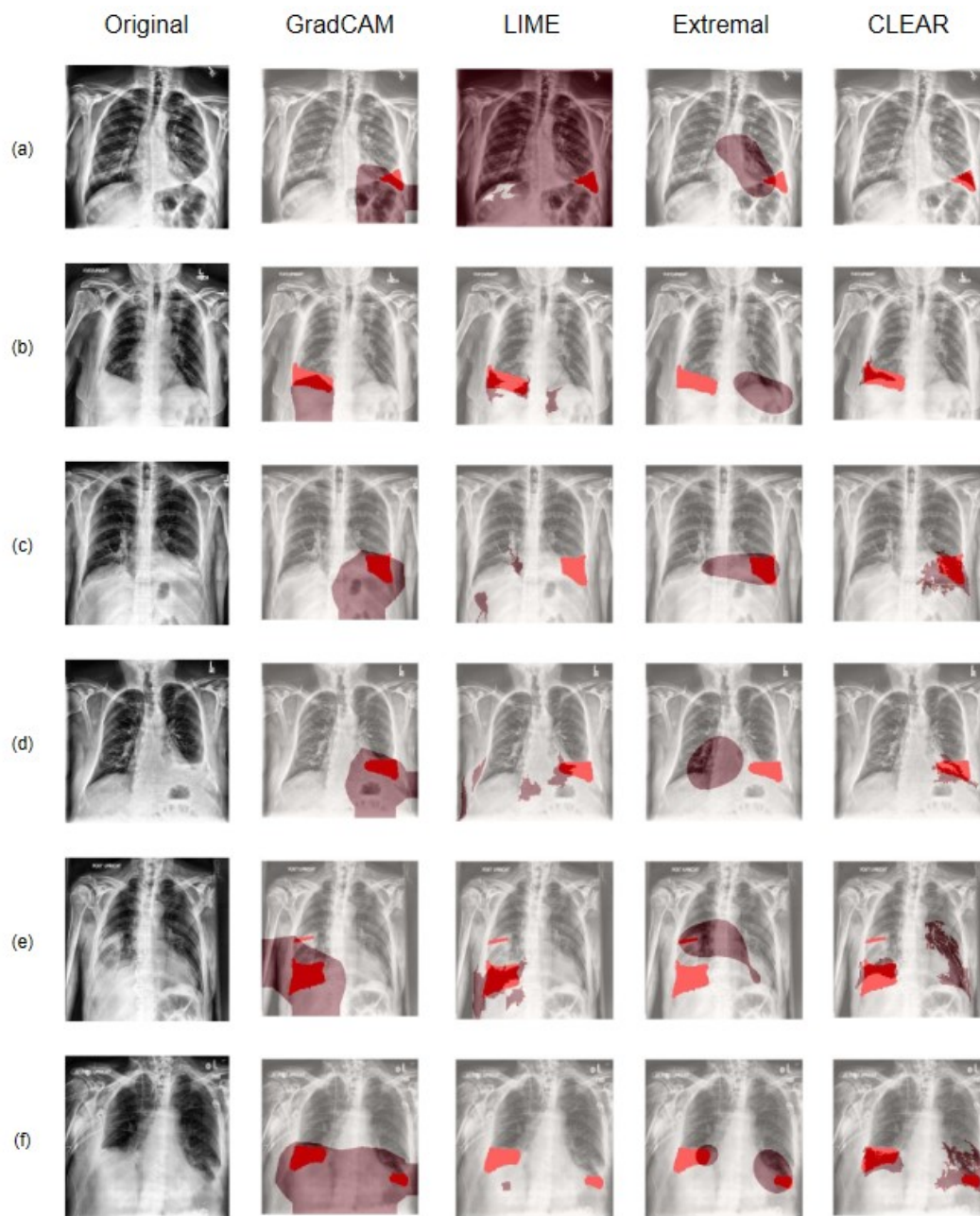
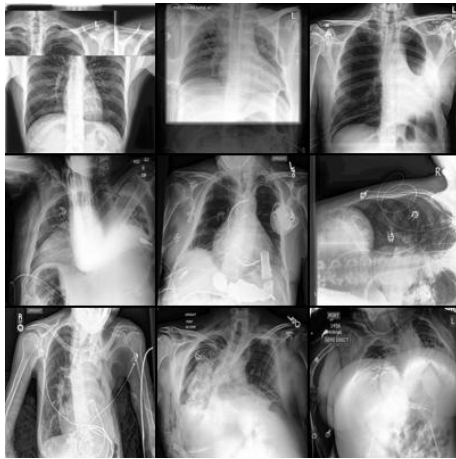


Figure 11: Representative comparative examples of the identified important segments of a VGG16-based image classification model (Val Acc: 97.5%) for pleural effusion using (i) CLEAR *Image*, (ii) Grad-CAM, (iii) Extremal Perturbation and (iv) LIME.

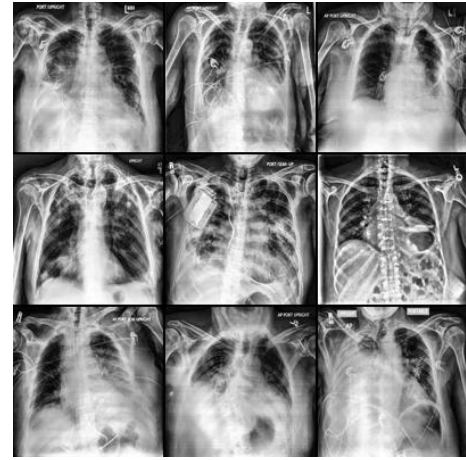


(a) Diseased

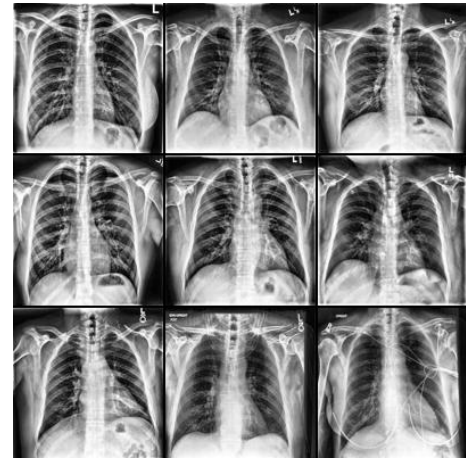


(b) Healthy

Figure 12: Representative examples of poorly curated images including image distortion, mis-orientation, obstruction by limbs and support devices as well as significant spine deformation.



(a) Diseased



(b) Healthy

Figure 13: Representative examples of final images for (a) diseased with identifiable regions of pathology and (b) healthy images with clear air space. All images have minimal obstructions from support devices.

## B Model Parameters

### B.1 DeScarGAN and Parameters

The DeScarGAN architecture was adopted for the synthetic dataset in Section 5.1. 80% of the dataset (4000 images) was used for GAN training and 20% of the dataset (1000 images) was used for validation. A total of 2,500 epochs was run and the best epoch was selected on visual quality. Additional 100 images were generated as an out-of-sample test dataset. Adam optimizer was used with  $\beta_1 = 0.5$ ,  $\beta_2=0.999$ . An initial learning rate of  $10^{-4}$  was used and stepped down to a final learning rate of  $10^{-6}$ . Default hyperparameters for loss functions were used to mimic a similar investigation from the original author as shown below in Table 1:

Loss Term	Weight Value
Adversarial Loss:	$\lambda_{adv,g} = 1$ (Generator) $\lambda_{adv,d} = 20$ (Discriminator)
Gradient Penalty Loss:	$\lambda_{gp} = 10$
Identity Loss:	$\lambda_{id} = 50$
Reconstruction Loss:	$\lambda_{rec} = 50$
Classification Loss:	$\lambda_{cls,g} = 1$ (Generator) $\lambda_{cls,d} = 5$ (Discriminator)

Table 1: Default Loss Function Hyperparameters used in DeScarGAN

### B.2 StarGAN-V2 and Parameters

StarGAN-V2 (Choi et al. 2020) has been adopted in this work as a state-of-art GAN network for image translation. Within this work, it has provided the necessary contrastive images for the CheXpert dataset. Default hyperparameters were maintained while notable loss weights are highlighted in Table 2. Adam optimizer was used with  $\beta_1 = 0$ ,  $\beta_2=0.99$ . A total of 50,000 epochs was run for the CheXpert dataset. The style encoding is referenced to the input image for the translation to the targeted class. This aids in maintaining the general features of the images compared to the original. As StarGAN-V2 (Choi et al. 2020) does not constrain its generation to a localised region (e.g. lungs), a post-processing of segmentation and blending was implemented for the CheXpert dataset. Segmentation of the lung region is based on a pre-trained model with a U-Net architecture. The segmentation mask is subsequently used to guide the replacement of pixels within the lung region from the GAN generated healthy image onto the original diseased image. Gaussian Blur is applied to minimise the edge effect during the blending process. This post-processing step aids in restricting the feature identification space within the lungs and reducing the computational cost for locating the counterfactuals.

Loss Term	Weight Value
Style Reconstruction Loss:	$\lambda_{sty} = 1$
Style Diversification Loss:	$\lambda_{ds} = 1$
Cyclic Loss:	$\lambda_{cyc} = 1$

Table 2: Default Loss Function Hyperparameters used in StarGANv2 (Choi et al. 2020)

### B.3 Clear Image and Parameters

The parameters for running CLEAR *Image* are in the script 'CLEAR\_settings.py'; this includes the random seed number parameter. This script can be found in our Code & Data appendix,

which also includes instructions for running CLEAR *Image*. The default parameters used for the Chest X-ray experiments were:

```
case_study = 'Medical'
max_predictors = 6
num_samples = 1000
regression_type = 'logistic'
logistic_regularise = False
score_type = 'aic'
apply_counterfactual_weights = True
counterfactual_weight = 200
binary_decision_boundary = 0.5
no_polynominals_no_interactions = True
interactions_only = True
no_intercept = False
centering = True
include_features = False
include_features_list = []
sufficiency_threshold = 0.99
image_infill = 'GAN'
image_all_segments = False
threshold_method = 'manual'
image_high_segment_threshold = 0.3
image_low_segment_threshold = 0.035
image_use_old_synthetic = False
image_counterfactual_interactions = False
image_segment_type = 'Augmented_GAN'
max_felz_segs_created_for_Augmented_GAN = 10
min_felz_segs_created_for_Augmented_GAN = 4
image_classes = ['normal', 'effusion']
```

For the CLEAR *Image* configuration experiments the parameter 'image\_infill' had values ['GAN', 'black'] and the parameter image\_segment\_type had values ['Augmented\_GAN', 'Felzenszwalb']

The same parameter values were used for the synthetic case study except:

```
case_study = 'Synthetic'
image_segment_type = 'Thresholding'
```